Quantum process tomography of a single solid state qubit

M Howard¹, J Twamley², C Wittmann³, T Gaebel³, F Jelezko³, and J Wrachtrup³

¹Dept. of Physics, University of California, Santa Barbara, CA 93106, U.S.A.

E-mail: jtwamley@ics.mq.edu

Abstract. We present an example of quantum process tomography (QPT) performed on a single solid state qubit. The qubit used is two energy levels of the triplet state in the Nitrogen-Vacancy defect in Diamond. Quantum process tomography is applied to a qubit which has been allowed to decohere for three different time periods. In each case the process is found in terms of the χ matrix representation and the affine map representation. The discrepancy between experimentally estimated process and the closest physically valid process is noted. The results of QPT performed after three different decoherence times are used to find the error generators, or Lindblad operators, for the system, using the technique introduced by Boulant et al. [6].

1. Introduction

Quantum process tomography (QPT) is a method of experimentally determining the unknown dynamics of a quantum system. This is crucial as a method of checking the functionality of would-be quantum information processing devices. Using knowledge obtained from QPT applied to such a device, one can ideally locate and possibly rectify any sources of errors or decoherence. The standard QPT technique, which involves the use of multiple test states, was first developed by Nielsen and Chuang [1] and Poyatos, Cirac and Zoller [2]. A different technique, exploiting entangled states, was subsequently proposed by Leung [3] and D'Ariano and Lo Presti [4]. More recently, methods have been developed to determine a process from a tomographically incomplete set of measurements [5], as well as techniques to ascertain the master equation describing time evolution of the system [6, 7]. QPT has been performed in liquid NMR implementations [8, 9, 10], numerous optical systems [11, 12, 13, 14, 15, 16], atoms in an optical lattice [17] and in bulk solid state NMR [18]. To the best of our knowledge, this work contains the first example of QPT performed on a single solid state qubit.

 $^{^2\}mathrm{Centre}$ for Quantum Computer Technology, Macquarie University, Sydney, New South Wales 2109, Australia

³University of Stuttgart, 3. Physical Institute, Stuttgart, Germany.

2. The Nitrogen Vacancy Defect in Diamond

The nitrogen vacancy defect (or N-V center) is a naturally occurring defect in diamond with nitrogen impurities. It can be manufactured in type IB synthetic diamond by irradiation and subsequent annealing at temperatures above 550 C; radiation damage causes vacancies in the diamond lattice and annealing leads to migration of vacancies towards the nitrogen atoms (see figure 1(a)). The N-V center can also be produced in type IIA diamonds by N⁺ ion implantation [19, 20].

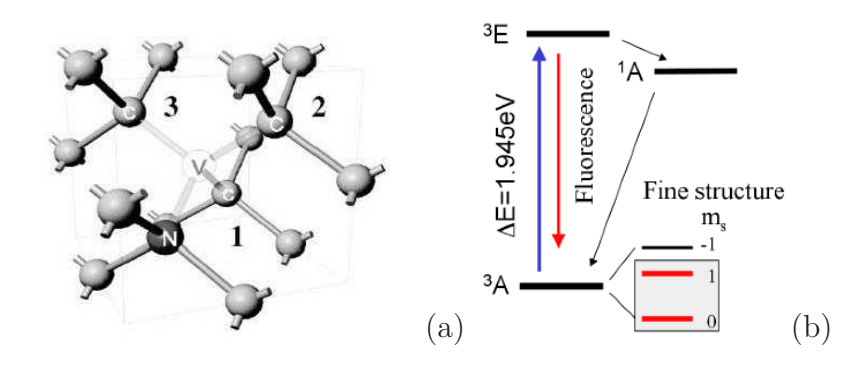


Figure 1. (a) Structure of the N-V defect (N=Nitrogen, V=Vacancy and C=Carbon) (b) Energy level scheme of N-V defect in a weak magnetic field. ${}^{3}E$ and ${}^{3}A$ are excited and ground triplet states respectively. The $m_s=0$ and $m_s=1$ states are used as a logical qubit

The energy level scheme of the N-V center is shown in figure 1(b). It consists of a triplet ground state 3A and a triplet excited state 3E with a metastable singlet state 1A . At zero magnetic field the ground triplet state energy levels are split into degenerate $m_s = \pm 1$ sublevels and the $m_s = 0$ sublevel. This is due to the magnetic dipole-dipole interaction between the 2 unpaired electrons. This dipole-dipole interaction can be described by a Hamiltonian term $H_D = \mathbf{S} \cdot \overline{D} \cdot \mathbf{S}$ where \overline{D} is the zero-field splitting (or fine structure) tensor and $\mathbf{S} = (S_x, S_y, S_z)$. Using standard techniques [22] this dipolar term can be rewritten as

$$H_D = D \left[S_z^2 - \frac{1}{3} S(S+1) \right] + E(S_x^2 + S_y^2), \tag{1}$$

where D and E are zero-field splitting parameters which are dependent on the symmetry of the molecule. The axial symmetry of the N-V center means that E = 0 MHz, while D for this system has previously been characterized [23, 24] as D = 2880 MHz. The end result is that, at zero magnetic field, the $m_s = \pm 1$ sublevels are degenerate and at an energy 2880 MHz greater than that of the $m_s = 0$ sublevel. With an applied magnetic field aligned along the z axis of the molecular system (i.e. $\vec{B} = (B_z, 0, 0)$) the total

Hamiltonian, including zero-field splitting term, takes the simple form

$$H_{Tot} = g\beta B_z S_z + D \left[S_z^2 - \frac{1}{3}S(S+1) \right],$$
 (2)

where the gyromagnetic ratio, $g\beta$, is 2.8025 MHz/Gauss. This Hamiltonian leads to a $|0\rangle \leftrightarrow |1\rangle$ transition of energy

$$\Delta E = (2,880 + 2.8025B_z)\text{MHz} \tag{3}$$

where B_z is the applied magnetic field (figure 2(a)), measured in Gauss.

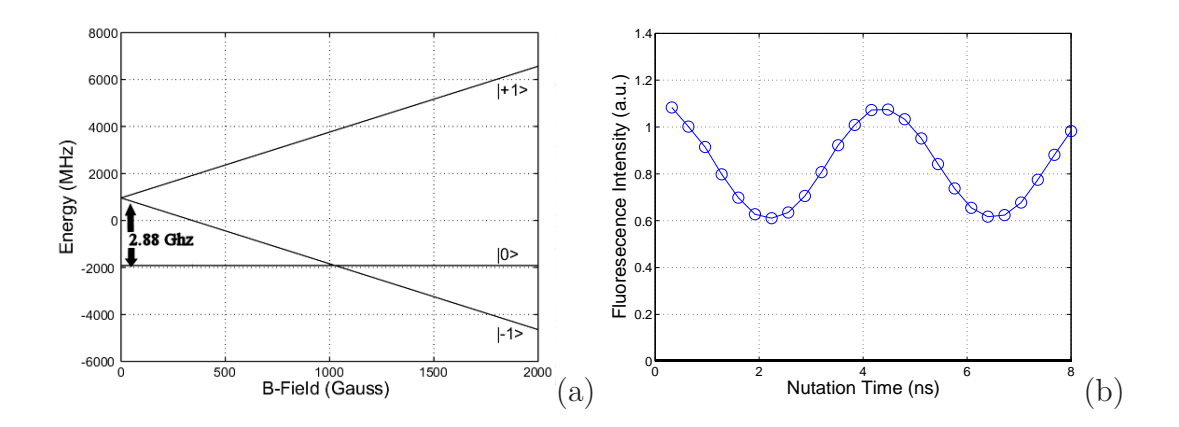


Figure 2. (a) Energy level schematic of spin S=1 triplet in an applied magnetic field. Because of the axial symmetry of the N-V defect, the $m_S = \pm 1$ sublevels remain degenerate in zero field and are split in non-zero magnetic field. (b) State readout is via Rabi oscillations of fluorescence intensity. The circles represent experimentally measured data points.

The fluorescence intensity corresponding to the $m_s = 0$ transition between the ground (3A) and excited (3E) triplet states is strongest. Optically detected magnetic resonance (ODMR) is used to perform state readout [25, 26, 27], i.e. the population of the $m_s = 0$ sublevel is identified by the amount of measured fluorescence (figure 2(b)). Manipulation of the qubit state is via standard electron spin resonance (ESR) techniques, using microwave pulses resonant with the $|0\rangle \leftrightarrow |1\rangle$ transition (3).

The spin longitudinal relaxation time, T_1 , is on the order of milliseconds at room temperature [28] (relaxation time of the order of seconds is expected at low temperature). Transverse relaxation times (or decoherence times), T_2 , of up to 60 microseconds have been reported [29], for samples with low nitrogen concentration.

In the N-V center, initialization into the $m_s = 0$ state is achieved by optical pumping. Optically induced spin polarization is thought to be related to spin-selective intersystem crossing from the photoexcited 3E triplet state to the metastable 1A singlet state (Figure 1(b)) i.e there is an irreversible transition between ${}^3E \to {}^1A$. The spin polarization achieved by this pumping corresponds to at least 70% population in the

 $m_s=0$ sublevel at room temperature. Instead of a pure state, corresponding to 100% polarization, we have what is known as a pseudopure state which takes the general form

$$\rho_{pseudo} = \left(\frac{1-\alpha}{2^n}\right) \mathbb{I} + \alpha |\psi\rangle\langle\psi| \tag{4}$$

where n is the number of qubits and $0 < \alpha < 1$ is related to the amount of polarization.

In the case of the N-V center, the 70% population of the $m_s = 0$ sublevel, after optical pumping, corresponds to $\text{Tr}(\rho_{pseudo}|0\rangle\langle 0|) = .7$ and so

$$\rho_{pseudo} = .6\left(\frac{\mathbb{I}}{2}\right) + .4|\psi\rangle\langle\psi|. \tag{5}$$

It is hoped that, in future experiments, the use of projective readouts, which are possible at low temperatures, will lead to increased polarizations.

A controlled two-qubit quantum gate in which the vacancy electron spin is hyperfine coupled to a nearby C^{13} nucleus, has recently been performed using this system [30].

3. Standard QPT

3.1. QPT Technique

We briefly review the standard QPT technique:

- Prepare a complete basis of input states $\rho_1 \dots \rho_{d^2}$ (e.g. $\rho_j = |\psi_j\rangle\langle\psi_j|, |\psi_j\rangle = \{|0\rangle, |1\rangle, \frac{1}{\sqrt{2}}(|0\rangle + |1\rangle), \frac{1}{\sqrt{2}}(|0\rangle + i|1\rangle)\}$, for a single qubit)
- Apply the unknown process \mathcal{E} to each member ρ_i
- Reconstruct the output states $\mathcal{E}(\rho_i)$ using quantum state tomography

While each of the reconstructed $\mathcal{E}(\rho_j)$ will be physically valid density matrices (by appropriate use of quantum state tomography) it is possible that the process \mathcal{E} describes is unphysical e.g. the $\mathcal{E}(\rho_j)$ are mutually inconsistent or \mathcal{E} is not completely positive. Experimental noise and a finite number of measurements to determine expectation values can result in a reconstructed \mathcal{E} which is not physically valid.

If it is possible to write a process in the Kraus representation then we can be sure it represents a physically valid process (one that is described by a completely positive map). We can specify an unknown process \mathcal{E} by experimentally determining the Kraus operators [31] $\{E_i\}$ which describe it

$$\mathcal{E}(\rho) = \sum_{i=1}^{d^2} E_i \rho E_i^{\dagger}. \tag{6}$$

or, using a fixed (complete) basis of operators $\{A_i\}$

$$\mathcal{E}(\rho) = \sum_{m,n=1}^{d^2} \chi_{mn} A_m \rho A_n^{\dagger}. \tag{7}$$

 χ_{mn} is a matrix of coefficients which completely describes the process \mathcal{E} and is positive Hermitean by construction. The trace preserving constraint $\sum_i E_i^{\dagger} E_i = \mathbb{I}$ becomes $\sum_{m,n} \chi_{mn} A_n^{\dagger} A_m = \mathbb{I}$.

- From the measurement results $\{\mathcal{E}(\rho_1)\dots\mathcal{E}(\rho_{d^2})\}$, λ_{jk} can be determined, given the relation $\mathcal{E}(\rho_j) = \lambda_{jk}\rho_k$.
- In order to determine χ from the matrix λ one operates on λ with the pseudoinverse of β , where β is derived theoretically from the relation $\hat{A}_m \rho_j \hat{A}_n^{\dagger} = \beta_{jk}^{mn} \rho_k$.
- Using this last relation and (7) we can see $\lambda_{ij} = \sum_{mn} \beta_{ij}^{mn} \chi_{mn}$ and so inverting β gives us χ , as required.

To derive $\{E_i\}$ from χ we first diagonalize χ with a unitary U^{\dagger}

$$\chi_{mn} = \sum_{k,l} U_{mx} d_k \delta_{kl} U_{nl}^* \tag{8}$$

where d_i are the eigenvalues of χ . The Kraus operators can then be obtained by

$$E_i = \sqrt{d_i} \sum_j U_{ji} A_j \tag{9}$$

Note that this procedure only works if $d_i \geq 0$ which follows from the positivity (semidefinite) of χ . It is this property which we use to check the physicality of a process \mathcal{E} ; if the χ matrix reconstructed from experimental data has negative eigenvalue(s) then this indicates that noise and/or finitely sampled expectation values has caused the output data to infer an unphysical process. To overcome this problem, a physical matrix $\tilde{\chi}$ is found which is as close as possible to the original χ in some sense. Specifically, we used a technique analogous to MLE for state estimation [21, 14] by minimising a deviation function, $\Delta(t)$, incorporating a general parameterization for a positive $\tilde{\chi}$:

$$\Delta(t) = \sum_{m,n=1}^{d^2} |\tilde{\chi}_{mn}(t) - \chi_{mn}|^2 + \lambda \left| \sum_{m,n=1}^{d^2} \tilde{\chi}_{mn}(t) A_n^{\dagger} A_m - \mathbb{I} \right|^2$$
 (10)

where λ is a Lagrange multiplier (which ensures a trace-preserving process) and

$$\tilde{\chi} = T^{\dagger}(t)T(t) \tag{11}$$

where T(t) is a $d^2 \times d^2$ complex, lower triangular matrix with d^4 real parameters, t(i). In the case of a single qubit we have:

$$T(t) = \begin{pmatrix} t(1) & 0 & 0 & 0 \\ t(5) + it(6) & t(2) & 0 & 0 \\ t(11) + it(12) & t(7) + it(8) & t(3) & 0 \\ t(15) + it(16) & t(13) + it(14) & t(9) + it(10) & t(4) \end{pmatrix}.$$
(12)

The algorithm used to minimise $\Delta(t)$ in (10) was the Nelder-Mead simplex algorithm as implemented in Matlab \mathbb{R} .

3.2. Avoiding Local Minima

As is often the case with numerical minimization problems, (10) typically contains numerous local minima. Our preliminary investigations suggested that, given a random initial point in parameter space, the algorithm would often fail to find the global minimum. As such, a good starting point, $t^*(i)$, in (12) was deemed necessary if the results were to be meaningful. In order to obtain $t^*(i)$ we used a technique based on principal component analysis [35]. If the experimentally determined matrix χ is not positive semidefinite, one can "filter" it by setting any (presumably quite small) negative eigenvalues to zero. Specifically, if we decompose χ as

$$\chi = UDU^{\dagger},\tag{13}$$

where D is a diagonal matrix containing the eigenvalues of χ , then we can construct a similar but positive matrix χ^* via

$$\chi^{\bigstar} = UD^{\bigstar}U^{\dagger},\tag{14}$$

where D^{\bigstar} is identical to D except that any negative eigenvalues have been set equal to zero. From χ^{\bigstar} we can extract good initial parameters $t^{\bigstar}(i)$ by performing a Cholesky decomposition (e.g. using the in-built "Chol" function in Matlab \mathbb{R}).

3.3. Process Visualisation

Any one qubit state can be parameterized by a so-called Bloch vector \vec{r} . Equivalently, one can explicitly include the unit coefficient of the identity basis component and parameterise the qubit state by a 4-vector $(1, r_x, r_y, r_z)^T$:

$$\rho = \frac{1}{2} \left(\mathbb{I} + \vec{r} \cdot \vec{\sigma} \right) \longleftrightarrow \frac{1}{2} \begin{pmatrix} 1 \\ r_x \\ r_y \\ r_z \end{pmatrix}$$
 (15)

where $r_x^2 + r_y^2 + r_z^2 \le 1$ [5]. In this basis any linear trace-preserving evolution \mathcal{E} takes the affine form

$$\mathcal{E}_{\mathcal{A}} = \begin{pmatrix} 1 & 0 \\ \vec{t} & E \end{pmatrix} = \begin{pmatrix} 1 & 0 & 0 & 0 \\ t_{x} & E_{xx} & E_{yx} & E_{zx} \\ t_{y} & E_{xy} & E_{yy} & E_{zy} \\ t_{z} & E_{xz} & E_{yz} & E_{zz} \end{pmatrix}, \tag{16}$$

and the process applied to an arbitrary input state is an affine map on \vec{r} , (although it remains a linear map on ρ):

$$\begin{pmatrix} 1 & 0 \\ \vec{t} & E \end{pmatrix} \begin{pmatrix} 1 \\ \vec{r} \end{pmatrix} = \begin{pmatrix} 1 \\ E\vec{r} + \vec{t} \end{pmatrix} = \begin{pmatrix} 1 \\ \vec{r'} \end{pmatrix}, \tag{17}$$

or, more explicitly,

$$\mathcal{E}_{\mathcal{A}}(\vec{r}) = \vec{r'} = E\vec{r} + \vec{t}. \tag{18}$$

Identifying the surface of the unit Bloch sphere as the set of all possible input states, we can visualize a process \mathcal{E} by its action on the sphere. The 3×3 matrix E is responsible for deformation and rotation of the Bloch sphere, while \vec{t} denotes displacement from $\vec{r} = (0, 0, 0)$.

We can gain crude but immediate insight into the nature of a single qubit process by using this visualization technique. Bloch vectors with $|\vec{r}| > 1$ do not correspond to any valid density matrix. Hence, when a process is depicted this way, any protrusions of the output ellipsoid outside the unit Bloch sphere mean that the process is not trace preserving.

Complete positivity also places constraints on physically allowable output ellipsoids. For a more detailed analysis of this problem we refer to [36, 37, 38]. The crucial point to note is that seemingly innocuous ellipsoids (i.e. contained within the unit Bloch sphere and not overly deformed) can represent a process which is not physically valid. The variety of allowable ellipsoids is particularly reduced when the translation vector \vec{t} in $\mathcal{E}_{\mathcal{A}}$ is non-zero.

4. Experimental Method

The QPT experiment was performed at room temperature using diamond nanocrystals obtained from type Ib synthetic diamond. Diamond nanocrystals were spin coated on a glass substrate, and single nanocrystals were observed with a homebuilt sample-scanning confocal microscope. In order to ensure the presence of a single defect in the laser focus, the second-order coherence was measured using Hanbury-Brown and Twiss interferometer and the contrast of the antibunching depth was determined. In order to perform many repetitions (to obtain good expectation values) in a reasonable amount of time, a sample with a relatively short coherence time $(2\mu s)$ was chosen. Microwaves were coupled to the sample by a ESR microresonator connected to a 40W travelling wave tube amplifier. A magnetic field $(\vec{B} = (0, 0, B_z), B_z = 200 \text{ Gauss})$ was applied to the defect in order to remove degeneracy of the $|\pm 1\rangle$ energy levels.

Rabi oscillations of fluoresence intensity were used to obtain expectation values. A reference nutation was initially taken in order to normalize the measurement nutations (i.e. set 0,1 levels for expectation values for the pseudopure initial state). In addition this reference oscillation was used to derive the microwave pulse time required to perform $\frac{\pi}{2}$ and π rotations of the Bloch vector. A complete basis of four input states was then prepared using microwave pulses resonant with qubit transitions. The ρ_0 state was obtained directly by optical pumping and three remaining input states ρ_1 , ρ_2 and ρ_3 were obtained by application of suitable π or $\frac{\pi}{2}$ pulses. Each of these states was left to decohere for a series of time intervals τ . As a last step, measurements of the diagonal and off-diagonal elements of the density matrix were performed.

Estimates of the density matrix elements were extracted from experimental data (Rabi oscillations) using the maximum entropy (MaxEnt) technique [39]. This method returns a physically valid density matrix which satisfies, as closely as possible, the

expectation values of measured observables. In cases where only incomplete knowledge of the output state is known, an additional constraint is used; the reconstructed state must also have the maximum allowable von Neumann entropy.

5. Quantum process tomography experiment

In summary the QPT experiment was performed as follows:

• The N-V center was optically pumped to the initial pseudopure state

$$\varrho_{pseudo} = .6\left(\frac{\mathbb{I}}{2}\right) + .4|0\rangle\langle 0| \tag{19}$$

Hereafter we neglect the identity component and treat this initial state as $\rho = |0\rangle\langle 0|$.

- Following this, each of the following input states $\rho_1 \dots \rho_{d^2}$ $(\rho_j = |\psi_j\rangle\langle\psi_j|, |\psi_j\rangle = \{|0\rangle, |1\rangle, \frac{1}{\sqrt{2}}(|0\rangle + |1\rangle), \frac{1}{\sqrt{2}}(|0\rangle + i|1\rangle)\}$ was created by application of suitable π or $\frac{\pi}{2}$ pulses.
- Each input state was then left to decohere, solely by interaction with its surroundings (i.e. no microwave (ESR) or optical (ODMR) radiation was applied to the system), for a decoherence time, τ .
- After τ had elapsed, expectation values for $\hat{\sigma_x}, \hat{\sigma_y}$ and $\hat{\sigma_z}$ were obtained by ODMR.
- Using $<\hat{\sigma_x}>,<\hat{\sigma_y}>$ and $<\hat{\sigma_z}>$ the final (output) states $\mathcal{E}(\rho_i)$, after the decoherence, were reconstructed via the MaxEnt technique.
- Using these output states, the process for each time period was reconstructed using the technique described above i.e. minimization of (10)

The processes, both from raw data and reconstructed (i.e. completly positive), are depicted in figures 5 to 5.

5.1. Quantification of Unphysicality

The Jamiolkowski isomorphism [32] maps a quantum operation \mathcal{E} , acting on \mathcal{H}_d , to a quantum state $\rho_{\mathcal{E}}$ in \mathcal{H}_{d^2} via

$$\rho_{\mathcal{E}} \equiv \left[\mathbb{I}_d \otimes \mathcal{E} \right] (|\Phi\rangle \langle \Phi|) \tag{20}$$

where $|\Phi\rangle\langle\Phi|$ is a projector on to a maximally entangled state in \mathcal{H}_{d^2} i.e.

$$|\Phi\rangle = \sum_{j} \frac{|j\rangle|j\rangle}{\sqrt{d}} \tag{21}$$

where $\{|j\rangle\}$ is some orthonormal basis set.

When the process \mathcal{E} is physical, one then obtains a physically valid $\rho_{\mathcal{E}}$ which can be compared to the ideal process (converted to ρ_{id}) using distance measures on quantum states [33]. The **trace distance** between density matrices ρ_{id} and $\rho_{\mathcal{E}}$ is

$$D(\rho_{id}, \rho_{\mathcal{E}}) \equiv \frac{1}{2} tr \mid \rho_{id} - \rho_{\mathcal{E}} \mid, \tag{22}$$

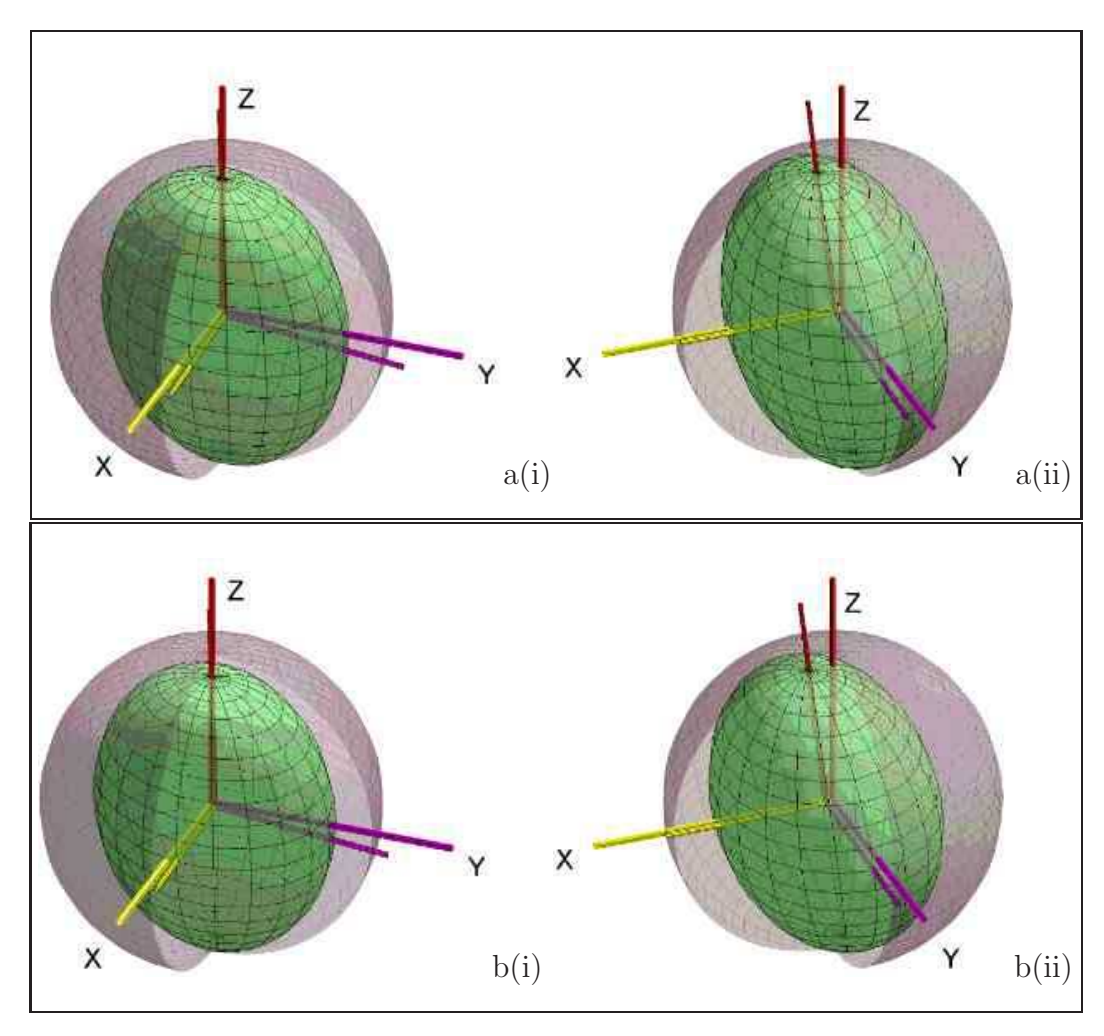


Figure 3. 20ns results: (a) Process from experimental data, χ . (b) Process obtained from physically valid $\tilde{\chi}$.

	Process Matrix $\mathcal{E}_{\mathcal{A}}$					
Experimental	(1.0000 0 0 0)					
	0.0626 0.6552 -0.0225 -0.1198					
	0.0448 0.0287 0.7309 -0.0226					
	$\left(\begin{array}{cccc} 0.0138 & -0.0143 & 0.0878 & 0.9843 \end{array}\right)$					
Reconstructed	(1.0000 0 0 0					
	0.0532 0.6798 -0.0312 -0.1093					
	0.0420 0.0206 0.7051 -0.0227					
	0.0070 0.0001 0.0916 0.9410					

where

$$\mid X \mid \equiv \sqrt{X^{\dagger}X}.\tag{23}$$

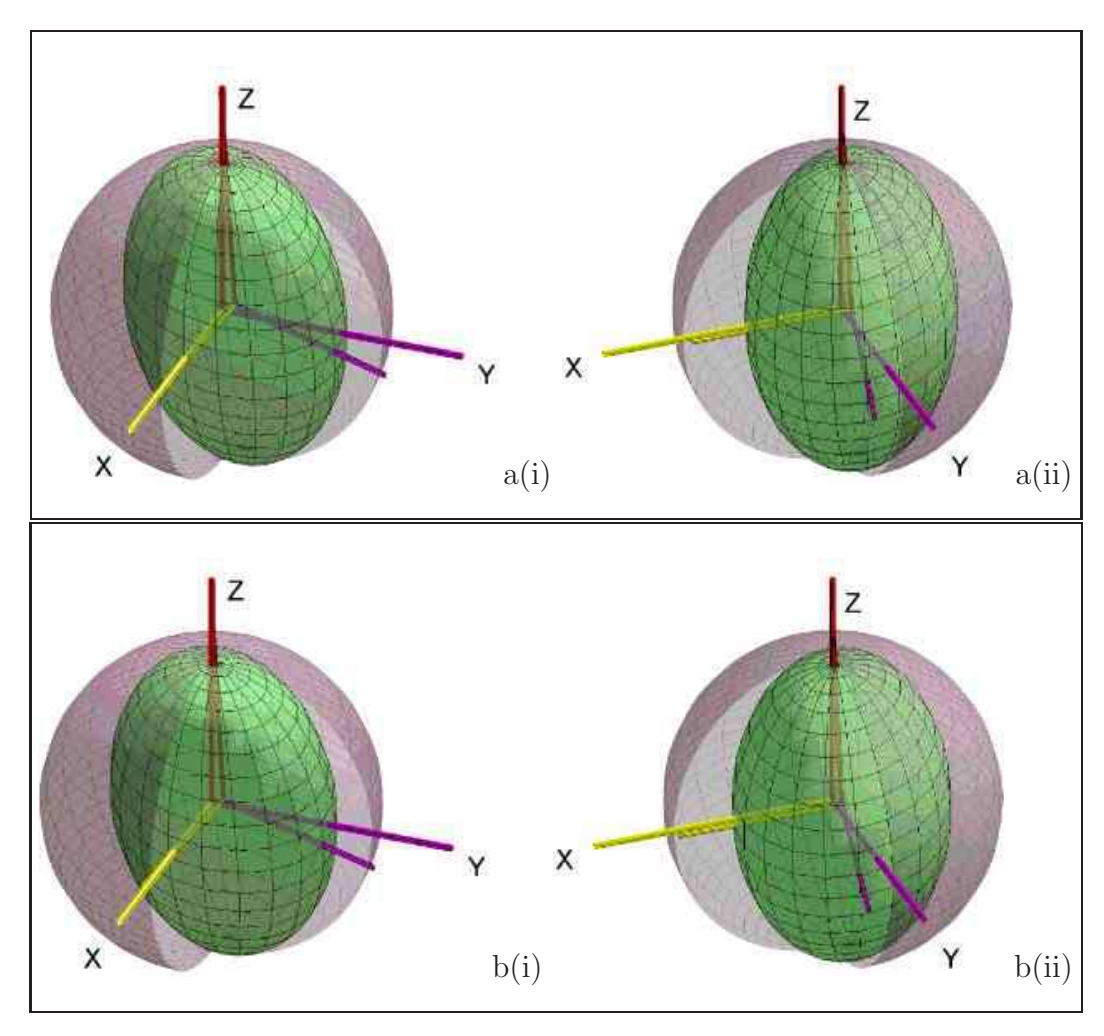


Figure 4. 40ns results: (a) Process from experimental data, χ . (b) Process obtained from physically valid $\tilde{\chi}$.

	Process Matrix $\mathcal{E}_{\mathcal{A}}$						
Experimental	$\begin{pmatrix} 1.0000 & 0 & 0 & 0 & \end{pmatrix}$						
	-0.0344 0.6378 0.1660 -0.0261						
	0.0683 -0.0728 0.6872 0.0499						
	$\left(\begin{array}{cccc} 0.0277 & 0.0536 & 0.0827 & 0.9614 \end{array}\right)$						
Reconstructed	$\begin{pmatrix} 1.0000 & 0 & 0 & 0 & \end{pmatrix}$						
	-0.0307 0.6477 0.1443 -0.0266						
	0.0638 -0.0944 0.6773 0.0407						
	$\begin{pmatrix} -0.0004 & 0.0532 & 0.0824 & 0.9320 \end{pmatrix}$						

Similarly one can define the **Fidelity**:

$$F(\rho_{id}, \rho_{\mathcal{E}}) \equiv tr \left(\sqrt{\sqrt{\rho_{id}} \rho_{\mathcal{E}} \sqrt{\rho_{id}}} \right)^{2}.$$
 (24)

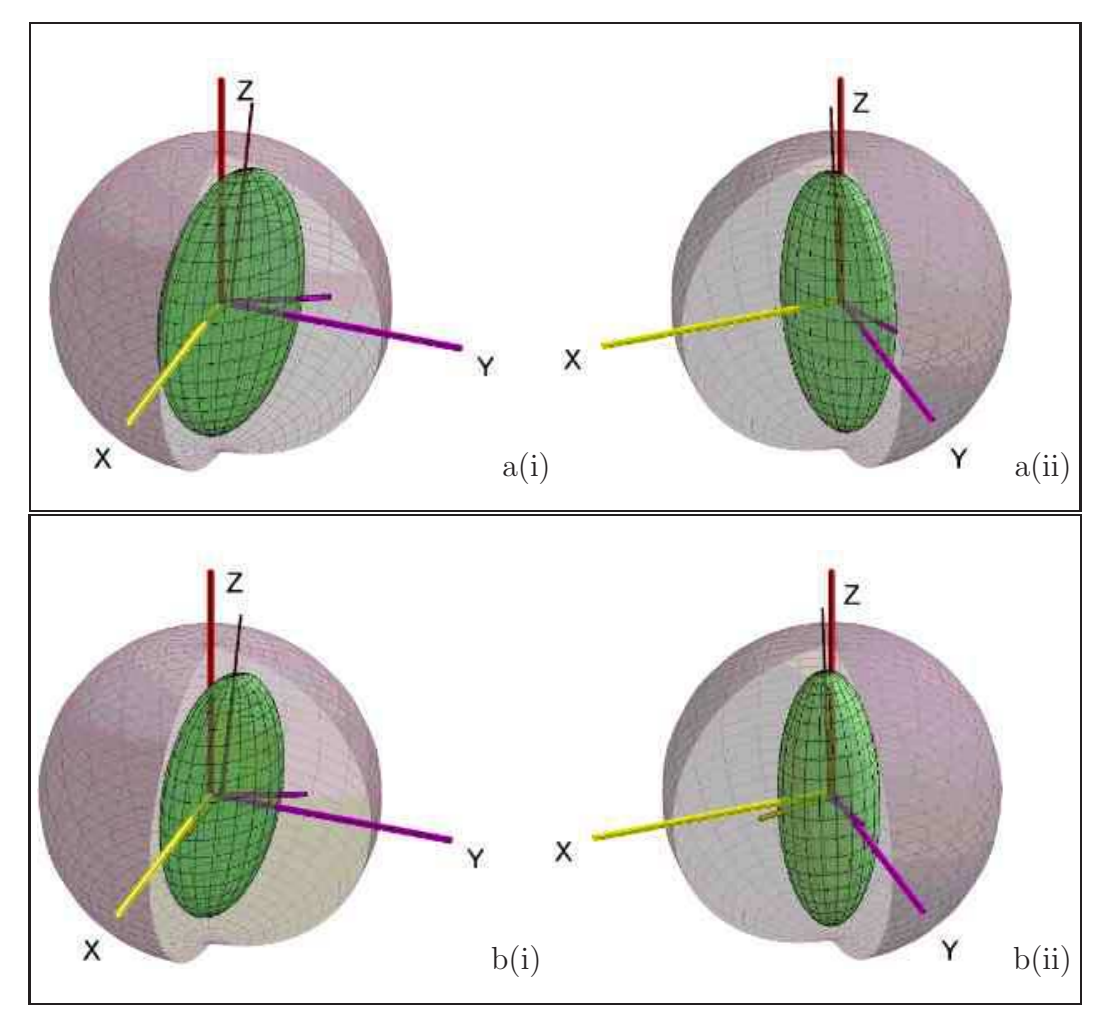


Figure 5. 80ns results: (a) Process from experimental data, χ . (b) Process obtained from physically valid $\tilde{\chi}$.

	Process Matrix $\mathcal{E}_{\mathcal{A}}$						
Experimental	(1.0000 0 0 0)						
	0.0442 0.2359 -0.1001 -0.0757						
	0.0791 -0.0947 0.3770 -0.1163						
	$\left(\begin{array}{cccc} 0.0434 & 0.0487 & -0.0461 & 0.9554 \end{array}\right)$						
Reconstructed	1.0000 0 0						
	0.0503 0.2726 -0.0290 -0.0752						
	0.0834 -0.0357 0.3291 -0.1038						
	$\left(\begin{array}{cccc} 0.0302 & 0.0457 & -0.0495 & 0.8984 \end{array}\right)$						

Using this definition we define the ${\bf Bures\ Metric}$

$$B(\rho_{id}, \rho_{\mathcal{E}}) \equiv \sqrt{2 - 2\sqrt{F(\rho_{id}, \rho_{\mathcal{E}})}}$$
(25)

and the C Metric

$$C(\rho_{id}, \rho_{\mathcal{E}}) \equiv \sqrt{1 - F(\rho_{id}, \rho_{\mathcal{E}})}.$$
 (26)

An unphysical process, however, can lead to an unphysical $\rho_{\mathcal{E}}$, possibly resulting in a process fidelity which is greater than one. The application of the preceding fidelity-based distance measures can, therefore, produce nonsensical results. In such cases it is necessary to use other techniques in order to estimate the disparity between χ and $\tilde{\chi}$ for example. If one defines $X = \chi - \tilde{\chi}$, then possible measures are the matrix p-norms $(p = 1, 2, \infty)$ of X and the Frobenius norm of X ($||X||_{Fro}$) as well as the trace distance (D_{pro}) .

As stated above, these quantities gives a measure of how well $\tilde{\chi}$ describes the experimental results. The difference matrix X varies depending on the basis of operators chosen for χ . We propose that if a standard basis is chosen then the norms of X, defined above, provide a method of "benchmarking" the quality of all such quantum process tomography experiments, regardless of implementation. Table 1 describes the discrepancies between experimental and reconstructed processes. Here we have chosen the normal basis $\{A_k\}(A_{di+j+1}=|i\rangle\langle j|)$ with which to construct χ and $\tilde{\chi}$. This particular choice of basis means that χ is equal to the Choi matrix \mathcal{C} [34, 6]

$$\chi = \mathcal{C} = \sum_{i,j=0}^{d-1} \mathcal{E}(|i\rangle\langle j|) \otimes |i\rangle\langle j|, \tag{27}$$

and proportional to the characteristic state $\rho_{\mathcal{E}}$ for the process:

$$\chi = d\rho_{\mathcal{E}} = d\left(\mathcal{E} \otimes \mathbb{I}_d\right) |\Phi\rangle\langle\Phi|. \tag{28}$$

Decoherence				
time	$ X _{p=1}$	$ X _{p=2}$	$ X _{Fro}$	D_{pro}
20ns	0.0660	0.0525	0.0636	0.0262
40ns	0.0581	0.0427	0.0529	0.0213
80ns	0.1141	0.1075	0.1276	0.0538

Table 1. The disparity between the estimated process from the experimental measurements (χ) and the "nearest" physically valid process $(\tilde{\chi})$. X is defined as $X = \chi - \tilde{\chi}$.

6. Markovian Process Tomography

Standard QPT utilises a "black box" approach to studying dynamics. It predicts the resultant output states given arbitrary initial states, but fails to describe the path taken through state space, over time, from initial to final state. If we are prepared to make certain assumptions about the relationship between system and environment, the Born and Markov approximations, then we can construct a Markovian quantum master equation which describes the time evolution of the system over the time studied. In the area of quantum information processing, understanding open system dynamics is important in studying quantum noise processes, designing error

correcting codes [40] and locating decoherence free subspaces [41]. We discuss a method of experimentally reconstructing a master equation by using estimates of the state of the system at a number of different timepoints. This particular technique was developed and implemented by Boulant, Havel, Pravia and Cory [6], in the context of liquid NMR quantum computation. The method is different to standard QPT techniques insofar as it assumes Markovian dynamics and, consequentially, the reconstructed equation has separate terms which describe the unitary and non-unitary aspects of the evolution. We then proceed to apply this technique to the N-V center, in an effort to better identify the decoherence processes it suffers. This is the first time such an analysis has been performed on a single solid state qubit.

By invoking the Born and Markov approximations one may derive the so-called **Lindblad Master Equation** [44], commonly expressed in a number of different but equivalent ways, including:

$$\frac{\partial \rho}{\partial t} = -i \left[H, \rho \right] + \frac{1}{2} \sum_{k=1}^{d^2 - 1} \left(2L_k \rho L_k^{\dagger} - L_k^{\dagger} L_k \rho - \rho L_k^{\dagger} L_k \right), \tag{29}$$

$$\frac{\partial \rho}{\partial t} = -i \left[H, \rho \right] + \frac{1}{2} \sum_{k=1}^{d^2 - 1} \left(\left[L_k \rho, L_k^{\dagger} \right] + \left[L_k, \rho L_k^{\dagger} \right] \right). \tag{30}$$

$$\frac{\partial \rho}{\partial t} = \hat{\mathcal{L}} \left[\rho \right] \tag{31}$$

The Lindblad master equation (30) is the diagonal form of the GKS master equation derived by Gorini, Kossakowski and Sudarshan [42]:

$$\frac{\partial \rho}{\partial t} = -i \left[H, \rho \right] + \frac{1}{2} \sum_{\alpha, \beta = 1}^{d^2 - 1} a_{\alpha\beta} \left(\left[F_{\alpha} \rho, F_{\beta}^{\dagger} \right] + \left[F_{\alpha}, \rho F_{\beta}^{\dagger} \right] \right)$$
(32)

where $a_{\alpha\beta}$ is a $(d^2-1)\times(d^2-1)$ Hermitean matrix and $\{F_{\alpha}\}$ is a linear basis of traceless operators on density matrices. If the matrix of coefficients $a_{\alpha\beta}$ (sometimes called the GKS matrix [43]) is positive, then the process described by (32) is completely positive. Diagonalising $a_{\alpha\beta}$ in (32) leads to the Linblad form (30).

We can clearly see one advantage gained by making the Born-Markov approximations - the resulting master equation can be separated into components which cause unitary and non-unitary evolution of the system:

Unitary Evolution:
$$-i[H, \rho],$$
 (33)

Non – Unitary Evolution :
$$\frac{1}{2} \sum_{k=1}^{d^2-1} \left(\left[L_k \rho, L_k^{\dagger} \right] + \left[L_k, \rho L_k^{\dagger} \right] \right). \tag{34}$$

The operators L_k are **Lindblad operators** and they describe the decoherence processes.

We now describe a technique for estimating the generator $\hat{\mathcal{L}}$ of a Markovian process. We transform to a Liouville space basis, as in [6], where density matrices become column vectors (denoted $|\rho\rangle$), and dynamical maps become $d^2 \times d^2$ matrix superoperators

Quantum process tomography of a single solid state qubit

14

(denoted by ^):

$$\frac{\partial |\rho\rangle}{\partial t} = \hat{\hat{\mathcal{L}}} |\rho\rangle. \tag{35}$$

The matrix superpropagator $\hat{P}(t)$ is then defined by exponentiation:

$$\underline{|\rho(t)\rangle} = e^{\hat{\mathcal{L}}t}\underline{|\rho(0)\rangle} = \hat{\mathcal{P}}(t)\underline{|\rho(0)\rangle}.$$
(36)

Henceforth we adopt a similar notation to [6]:

$$\frac{\partial \rho}{\partial t} = -i \left[H, \rho \right] + \frac{1}{2} \sum_{k=1}^{d^2 - 1} \left(\left[L_k \rho, L_k^{\dagger} \right] + \left[L_k, \rho L_k^{\dagger} \right] \right)$$
 (37)

becomes

$$\frac{\partial \underline{|\rho\rangle}}{\partial t} = -i\hat{\mathcal{H}}\underline{|\rho\rangle} - \hat{\mathcal{R}}\underline{|\rho\rangle}$$
(38)

$$= -\left(i\hat{\mathcal{H}} + \hat{\mathcal{R}}\right)\underline{|\rho\rangle} \tag{39}$$

We call $\hat{\mathcal{H}}$ the Hamiltonian superoperator and $\hat{\mathcal{R}}$ the relaxation superoperator. Exponentiating the generator gives us the superpropagator

$$\hat{\hat{\mathcal{P}}}(t) = e^{-\left(i\hat{\mathcal{H}} + \hat{\mathcal{R}}\right)t}.$$
(40)

We can manipulate (40) to isolate the relaxation superoperator:

$$\hat{\hat{\mathcal{R}}} = -i\hat{\mathcal{H}} - \frac{1}{t}\ln\left(\hat{\hat{\mathcal{P}}}\right) \tag{41}$$

An alternative method of deriving $\hat{\mathcal{R}}$ from estimates of $\hat{\mathcal{P}}$ and $\hat{\mathcal{H}}$ is to estimate the derivative at t=0 of

$$e^{\frac{t}{2}i\hat{\mathcal{H}}}e^{-\left(i\hat{\mathcal{H}}+\hat{\mathcal{R}}\right)t}e^{\frac{t}{2}i\hat{\mathcal{H}}}.$$
(42)

Here we need to invoke the symmetric Baker-Campbell-Hausdorff formula, for arbitrary operators A and B,

$$e^{\frac{t}{2}A}e^{tB}e^{\frac{t}{2}A} = e^{\left(t(A+B) - \frac{1}{24}t^3[A+2B,[A,B]] + O(t^5)\right)}.$$
(43)

Making the identification

$$A = i\hat{\mathcal{H}},\tag{44}$$

$$B = -\left(i\hat{\mathcal{H}} + \hat{\mathcal{R}}\right),\tag{45}$$

we get

$$e^{\frac{t}{2}i\hat{\mathcal{H}}}e^{-(i\hat{\mathcal{H}}+\hat{\mathcal{R}})t}e^{\frac{t}{2}i\hat{\mathcal{H}}} = e^{-t\hat{\mathcal{R}}} + O(t^3). \tag{46}$$

Clearly, differentiating (46) at t=0 gives us $\hat{\mathcal{R}}$, as required. In order to obtain this differential we used a numerical differentiation technique - Richardson extrapolation [45, 6].

To use this technique we require estimates of the propagator, $\hat{\mathcal{P}}_m = \hat{\mathcal{P}}(t_m)$, at time points $t_m = 2^m t_1$. This alone, however, is not a robust method for estimating $\hat{\mathcal{R}}$. It magnifies the noise present in the estimate of $\hat{\mathcal{P}}_1$ [6]. More importantly, there are no constraints on the physicality (i.e. complete positivity) of the generator. This estimate of $\hat{\mathcal{R}}$ which we will call $\hat{\mathcal{R}}_{RE}$ is instead used as the *starting point* for a constrained fit to the experimental data.

In order to search for a physical process which was close to the measured data we used a parameterisation based on the Gorini Kossakowski Sudarshan master equation:

$$\hat{\hat{\mathcal{L}}} = -i\left[H, \rho\right] + \frac{1}{2} \sum_{\alpha, \beta = 1}^{d^2 - 1} a_{\alpha\beta} \left(\left[F_{\alpha}\rho, F_{\beta}^{\dagger}\right] + \left[F_{\alpha}, \rho F_{\beta}^{\dagger}\right] \right). \tag{47}$$

Gorini et al. have proven [42] that $\hat{\mathcal{L}}$ is the generator of a Markovian semigroup on d-dimensional Hilbert space if and only if it can be written in the form (47), where the GKS matrix $a_{\alpha\beta}$ is a $(d^2-1)\times(d^2-1)$ positive (semidefinite) matrix and $\{F_{\alpha}\}$ is a linear basis of traceless operators on ρ . We will exploit the requirement that $a_{\alpha\beta}$ be positive in a way that is completely analogous to a technique we used in standard QPT. During process reconstruction we enforced positivity of $\tilde{\chi}$, and, by extension, the complete positivity of $\mathcal{E}(\rho)$. Similarly we will enforce complete positivity of the decoherence process $\hat{\mathcal{R}}$ by constraining the GKS matrix $a_{\alpha\beta}$ to be positive.

For one qubit we have a parameterisation in terms of 9 real numbers x(i):

$$-\hat{\mathcal{R}}(x(i)) = \frac{1}{2} \sum_{\alpha,\beta=1}^{d^2-1} a_{\alpha\beta}(x(i)) \left(\left[F_{\alpha}\rho, F_{\beta}^{\dagger} \right] + \left[F_{\alpha}, \rho F_{\beta}^{\dagger} \right] \right)$$
 (48)

where

$$a_{\alpha\beta}(x(i)) = \mathbb{X}^{\dagger}\mathbb{X}$$
 $\mathbb{X}(x) = \begin{pmatrix} x(1) & 0 & 0 \\ x(4) + ix(5) & x(2) & 0 \\ x(8) + ix(9) & x(6) + ix(7) & x(3) \end{pmatrix}$. (49)

There is considerable freedom in which basis $\{F_{\alpha}\}$ to use but we chose to use generators for SU(d), rescaled to be trace orthonormal:

$$F_1 = \frac{1}{\sqrt{2}} \begin{pmatrix} 0 & 1\\ 1 & 0 \end{pmatrix},\tag{50}$$

$$F_2 = \frac{1}{\sqrt{2}} \begin{pmatrix} 0 & -i \\ i & 0 \end{pmatrix}, \tag{51}$$

$$F_3 = \frac{1}{\sqrt{2}} \begin{pmatrix} 1 & 0 \\ 0 & -1 \end{pmatrix}. \tag{52}$$

A numerical search, using Matlab's® fminsearch algorithm, was used to find the minimum of

$$\Delta(\hat{\hat{\mathcal{R}}}(x)) = \sum_{m=1}^{M} \left| e^{-\left(i\hat{\hat{\mathcal{H}}} + \hat{\hat{\mathcal{R}}}(x)\right)t_m} - \hat{\hat{\mathcal{P}}}_m \right|^2$$
(53)

where $\hat{\hat{P}}_m$ are the experimentally determined propagators, for evolution time t_m i.e.

$$\hat{\hat{\mathcal{P}}_m} = \left[\left(\frac{|\rho_1(t_m)\rangle}{|\rho_2(t_m)\rangle} \right) \left(\frac{|\rho_2(t_m)\rangle}{|\rho_3(t_m)\rangle} \right) \left(\frac{|\rho_4(t_m)\rangle}{|\rho_4(t_m)\rangle} \right) \right]$$
(54)

where

$$\underline{|\rho_1(0)\rangle} = \begin{pmatrix} 1\\0\\0\\0 \end{pmatrix}, \ \underline{|\rho_2(0)\rangle} = \begin{pmatrix} 0\\1\\0\\0 \end{pmatrix}, \ \underline{|\rho_3(0)\rangle} = \begin{pmatrix} 0\\0\\1\\0 \end{pmatrix}, \ \underline{|\rho_4(0)\rangle} = \begin{pmatrix} 0\\0\\0\\1 \end{pmatrix}. (55)$$

We label the GKS matrix which most closely fits the data, while remaining physical, as $\widetilde{a_{\alpha\beta}}$ (see figures 6 and 7). To derive the Lindblad operators $\{L_k\}$ from $\widetilde{a_{\alpha\beta}}$ we first diagonalise $\widetilde{a_{\alpha\beta}}$ with a unitary U^{\dagger} ,

$$\widetilde{a_{mn}} = \sum_{xy} U_{mx} d_x \delta_{xy} U_{ny}^*, \tag{56}$$

where d_i are the eigenvalues of $\widetilde{a_{\alpha\beta}}$. The Lindblad operators can then be obtained by

$$L_i = \sqrt{d_i} \sum_j U_{ji} F_j. \tag{57}$$

These are depicted in figures 8 to 10. The expectation values $\langle \hat{\sigma_x} \rangle$, $\langle \hat{\sigma_y} \rangle$ and $\langle \hat{\sigma_z} \rangle$ for both the experimental and the reconstructed (Markovian, completely positive) process are compared in figure 11. It is natural now to ask given the estimations for L_i , whether one can deduce any information regarding the physical decoherence processes responsible. Unfortunately, this is not generally possible. The most general Markovian master equation for a qubit can be fully described by three Linblad operators. However this compressed description often will not correspond to the most appropriate physical description of the decoherence. It can be argued however, that in most situations, e.g. decoherence free subspace investigation, decoupling pulse generation etc., all the relevant information is contained in the compressed Lindblad description.

The relative contribution of each Lindblad operator, L_i , to the overall decoherence process can be quantified using their Frobenius norms:

Relative Contribution(L_i) =
$$\frac{|L_i|_{Fro}^2}{\sum_{i=1}^{d^2-1} |L_j|_{Fro}^2}.$$
 (58)

In summary the technique we used for ascertaining the relaxation superoperator $\hat{\hat{\mathcal{R}}}$ is as follows:

- Initialisation via optical pumping and appropriate ESR pulses to create a complete basis of input states ρ_i .
- Each ρ_i was left to decohere for a sequence of times $t_m = 2^m t_1$ i.e. {20ns, 40ns, 80ns}.

- State tomography was used to determine the output state $\rho_i(t_m)$ after each decoherence time t_m . The results were used to construct the matrix superpropagators \hat{P}_m .
- Using Richardson extrapolation, an estimate of the generator, $\hat{\mathcal{R}}_{RE}$, was extracted from the measured $\hat{\mathcal{P}}_m$ and used as a starting point for the fitting procedure (53).
- The minimisation of (53) produced a Markovian generator, $\hat{\mathcal{R}}$, which was physically valid and best fit the measured data at a sequence of timepoints t_m .
- The GKS matrix which minimised (53), $\widetilde{a}_{\alpha\beta}$, was then diagonalised in order to find the Lindblad operators $\{L_k\}$.

6.1. Markovian process tomography results

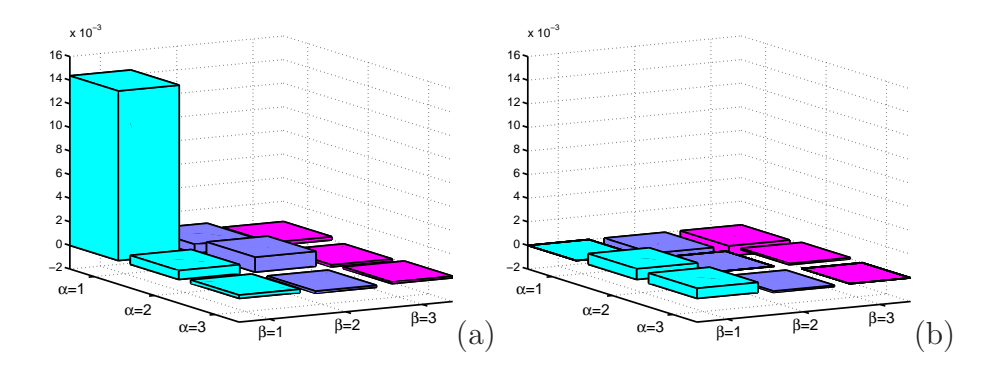


Figure 6. GKS matrix $a_{\alpha\beta}$: the initial starting point for minimization of (53) (a) Real components of $a_{\alpha\beta}$ (b) Imaginary components of $a_{\alpha\beta}$.

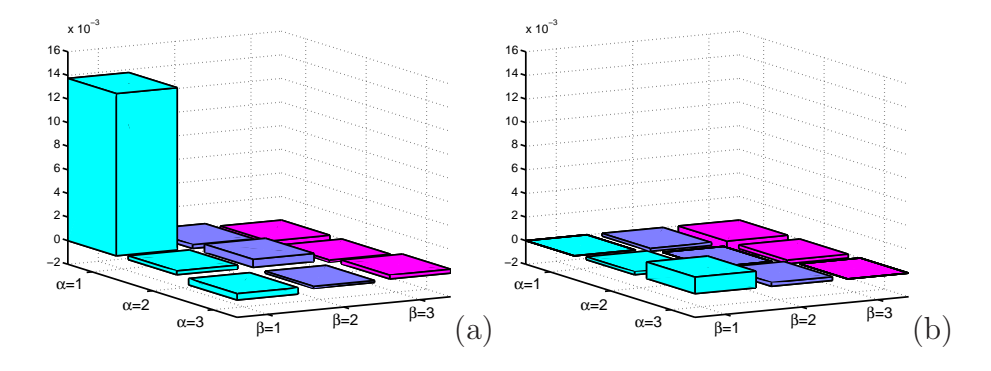


Figure 7. GKS matrix $\widetilde{a_{\alpha\beta}}$: the matrix which minimizes (53) (a) Real components of $\widetilde{a_{\alpha\beta}}$ (b) Imaginary components of $\widetilde{a_{\alpha\beta}}$.

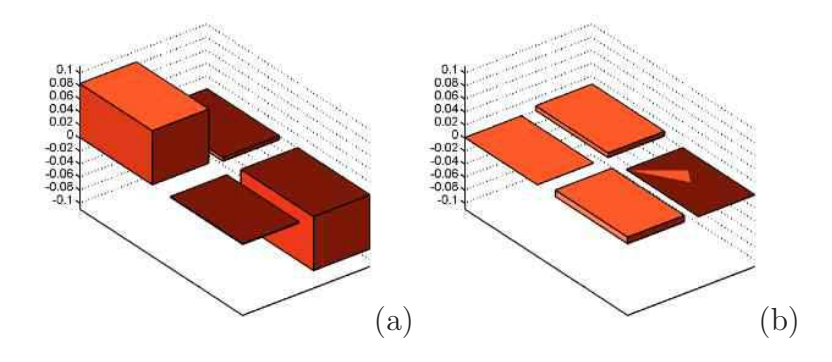


Figure 8. Lindblad operator L_1 , Relative contribution $\approx 94.4\%$: (a) Real components of L_1 . (b) Imaginary components of L_1 .

$$L_1 = \begin{pmatrix} 0.0829 - 0.0000i & -0.0056 - 0.0071i \\ -0.0011 + 0.0101i & -0.0829 + 0.0000i \end{pmatrix}$$

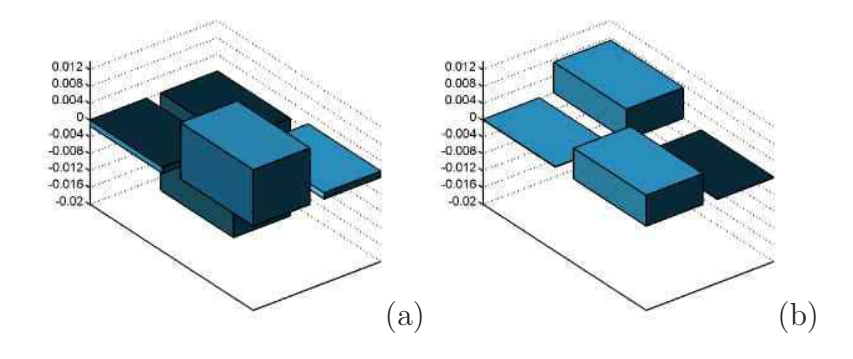


Figure 9. Lindblad operator L_2 , Relative contribution $\approx 5.6\%$: (a) Real components of L_2 . (b) Imaginary components of L_2 .

$$L_2 = \begin{pmatrix} -0.0014 + 0.0001i & -0.0232 + 0.0072i \\ 0.0134 + 0.0072i & 0.0014 - 0.0001i \end{pmatrix}$$

7. Summary

We have presented the first quantum process tomographic analysis of an individual single solid-state qubit, a Nitrogen Vacancy centre in Diamond. This analysis is only possible due to the enormous advances made in recent years in single-molecule spectroscopy [25, 26, 27], where the resultant ODMR technique provides us here with high-fidelity single-qubit readout. As experimental refinements and technological advances improve

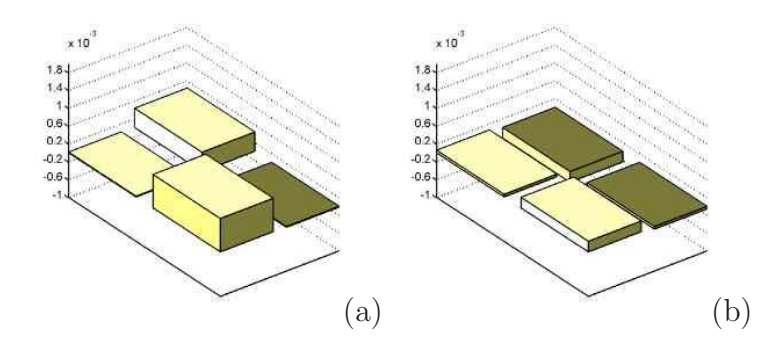


Figure 10. Lindblad operator L_3 , Relative contribution $\approx (1 \times 10^{-4}) \%$: (a) Real components of L_3 . (b) Imaginary components of L_3 .

$$L_3 = 1 \times 10^{-3} \begin{pmatrix} 0.0151 + 0.0577i & 0.4324 - 0.2377i \\ 0.7500 + 0.2377i & -0.0151 - 0.0577i \end{pmatrix}$$

the readout and control of this system, QPT will become an even more important diagnostic tool. For example, improvement of the $m_s = 0$ polarisation by optical pumping and increased accuracy of rotations by the use of composite pulse sequences, are both feasible short-term goals. If states can be prepared, controlled and read out with very high accuracy, then any deviations from Markovian dynamics (e.g. the disparity in expectation values, between experimental and reconstructed processes apparent in figure 11) cannot be dismissed as noise and the nature of the non-Markovian environment should be investigated. If two qubit gates can be performed in this system then QPT can be used to verify the robustness of encoded information in decoherence free subspaces. As quantum devices develop and increase in size, the task of "debugging" the device, or actively identifying the noise present in the device, will pose significant challenges. The work presented here represents an initial step towards the testing of quantum devices in solid-state.

References

- [1] Chuang I L and Nielsen M A 1997 J. Mod. Opt. 44 2455.
- [2] Poyatos F, Cirac J I and Zoller P 1997 Phys. Rev. Lett. 78 390.
- [3] Leung D W, Ph.D. Thesis 2000 Stanford University .
- [4] D'Ariano G M and Lo Presti P 2001 Phys. Rev. Lett. 86 4195.
- [5] Ziman M, Plesch M and Buzek V 2004 quant-ph /0406088.
- [6] Boulant N, Havel T F, Pravia M A and Cory D G 2003 Phys. Rev. A. 67 042322.
- [7] Buzek V 1998 Phys. Rev. A 58 1723.
- [8] Nielsen M A, Knill E and Laflamme R 1998 Nature 396 52.
- [9] Childs A M, Chuang I L and Leung D W 2001 Phys. Rev. A 64 012314.
- [10] Weinstein Y S et al. 2004 J Chem Phys. 121 6117.

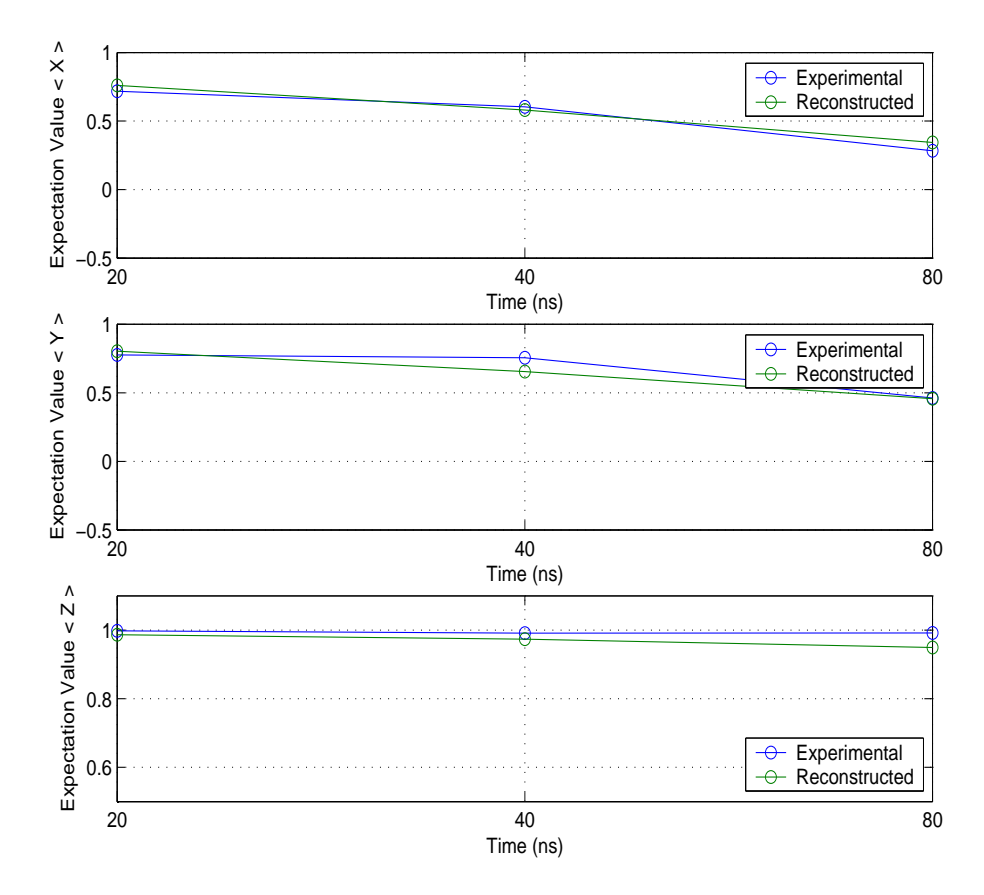


Figure 11. Comparison of experimental expectation values at timepoints t_m with expectation values predicted by Markovian master equation. The time is plotted on a logarithmic scale for clarity.

- [11] D'Ariano G M and Lo Presti P 2003 Phys. Rev. Lett. 91 047902.
- [12] Nambu Y et al. 2002 Proc. SPIE 4917 13.
- [13] De Martini F et al. 2003 Phys. Rev. A 67 062307.
- [14] O 'Brien J L et al. 2004 Phys. Rev. Lett 93 08025.
- [15] Mitchell M W et al. 2004 Phys. Rev. Lett 91 120402.
- [16] Altepeter J B et al. 2003 Phys. Rev. Lett **90** 193601.
- [17] Myrskog S H et al. 2003 quant-ph /0312210.
- [18] Kampermann H and Veeman W S 2002 Quantum Information Processing 1 Issue 5 327-344.
- [19] J. Meijer et al. 2005 App. Phys. Lett., in press, cond-mat /0505063.
- [20] J. R. Rabeau et al. 2005 App. Phys. Lett., in press.
- [21] Ježek M, Fiurášek J and Hradil Z 2003 Phys. Rev. A 68 012305.
- [22] Bersohn M and Baird J C 1966 An Introduction to Electron Paramagnetic Resonance (New York: W. A. Benjamin, Inc.) p114.
- [23] van Oort E, Ph.D. Thesis, Amsterdam 1990
- [24] Reddy N R S, Manson N B, and Krausz E R 1987 Journal of Luminescence 38 46.
- [25] Jelezko F et al. 2002 Appl. Phys. Lett. 81 2160.
- [26] Gruber A et al. 1997 Science **276** 2012.
- [27] Kurtsiefer C et al. 2000 Phys. Rev. Lett. 85 290.
- [28] Redman D A, Brown S, Sands D H and Rand S C 1991 Phys Rev. Lett. 67 3420.
- [29] Kennedy T A et al. 2003 Appl. Phys. Lett. 83 4190.
- [30] Jelezko F. et al. 2004 Phys. Rev. Lett. 93 130501.

- [31] Kraus K 1983 States, Effects and Operations: Fundamental Notions of Quantum Theory, Lecture Notes in Physics (Berlin: Springer-Verlag) 190.
- [32] Jamiolkowski A 1972 Rep. Math. Phys. **3** 275.
- [33] Gilchrist A, Langford N K and Nielsen M A 2004 quant-ph/0408063.
- [34] Choi M D 1975 Linear Algebra and its Applications 10 285.
- [35] Havel T F 2003 J. Math. Phys. 44 534.
- [36] Ruskai M B, Szarek S and Werner E 2002 Linear Algebra and its Applications 347 159.
- [37] Oi D K L 2001 quant-ph/0106035.
- [38] Fujiwara A and Algoet P 1999 Phys. Rev. A 59 3290.
- [39] Buzek V and Drobny G 2000 J. Mod. Opt. 47 2823-2840.
- [40] Gottesman D 1999 Proceedings of the 23rd International Colloquim on Group Theoretical Methods in Physics (Cambridge: International Press) p. 23.
- [41] Bacon D, Lidar D A, and Whaley K B 1999 quant-ph/9902041.
- [42] Gorini V, Kossakowski A, and Sudarshan E C G 1976 J. Math. Phys. 17 821.
- [43] Bacon D, Childs A M, Chuang I L, Kempe J, Leung D W, and Zhou X 2001 Phys. Rev. A 64 062302.
- [44] G. Lindblad, Comm. Math. Phys. 48, 119 (1976).
- [45] G. Dahlquist, and A. J. Bjorck, Numerical Methods [translated by N. Anderson], Prentice-Hall, New York (1974).